Reports of Practical Oncology and Radiotherapy 25 (2020) 738–745

Available online at www.sciencedirect.com

Reports of Practical Oncology and Radiotherapy

journal homepage: http://www.elsevier.com/locate/rpor

Original research article

# Estimation and evaluation of pseudo-CT images using linear regression models and texture feature extraction from MRI images in the brain region to design external radiotherapy planning

Niloofar Yousefi Moteghaed[a], Ahmad Mostaar[a,b,*], Keivan Maghooli[c], Mohammad Houshyari[d], Ahmad Ameri[e]

[a] Department of Biomedical Engineering and Medical Physics, Faculty of Medicine, Shahid Beheshti University of Medical Sciences, Tehran, Iran
[b] Radiation Biology Research Center, Iran University of Medical Sciences, Tehran, Iran
[c] Department of Biomedical Engineering, Islamic Azad University, Science and Research Branch, Tehran, Iran
[d] Department of Radiation Oncology, Shohada-e-Tajrish Hospital, Faculty of Medicine, Shahid Beheshti University of Medical Sciences, Tehran, Iran
[e] Department of Radiation Oncology, Imam Hossein Hospital, Faculty of Medicine, Shahid Beheshti University of Medical Sciences, Tehran, Iran

ARTICLE INFO

*Article history:*
Received 3 January 2020
Received in revised form 5 May 2020
Accepted 25 May 2020
Available online 11 July 2020

*Keywords:*
MRI-only treatment planning
Pseudo-CT
Polynomial regression model
Dose evaluation

ABSTRACT

*Aim:* The aim of this study is to construct and evaluate Pseudo-CT images (P-CTs) for electron density calculation to facilitate external radiotherapy treatment planning.
*Background:* Despite numerous benefits, computed tomography (CT) scan does not provide accurate information on soft tissue contrast, which often makes it difficult to precisely differentiate target tissues from the organs at risk and determine the tumor volume. Therefore, MRI imaging can reduce the variability of results when registering with a CT scan.
*Materials and methods:* In this research, a fuzzy clustering algorithm was used to segment images into different tissues, also linear regression methods were used to design the regression model based on the feature extraction method and the brightness intensity values. The results of the proposed algorithm for dose-volume histogram (DVH), Isodose curves, and gamma analysis were investigated using the RayPlan treatment planning system, and VeriSoft software. Furthermore, various statistical indices such as Mean Absolute Error (MAE), Mean Error (ME), and Structural Similarity Index (SSIM) were calculated.
*Results:* The MAE of a range of 45–55 was found from the proposed methods. The relative difference error between the PTV region of the CT and the Pseudo-CT was 0.5, and the best gamma rate was 95.4% based on the polar coordinate feature and proposed polynomial regression model.
*Conclusion:* The proposed method could support the generation of P-CT data for different parts of the brain region from a collection of MRI series with an acceptable average error rate by different evaluation criteria.



## 1. Background

The goal of external radiotherapy (RT) is to eliminate cancer cells using high-energy ionizing radiation. To this end, radiation attenuation properties should be known in different tissues in order to calculate the three-dimensional (3D) dose distribution. CT scan images, given the direct relationship with the electron density of the tissue being imaged, and provides accurate geometry of the bone to present digitally reconstructed radiographs (DRRs). In recent years the advantages of MRI have been presented in the design process.[1,2] MRI imaging creates high contrast in soft tissues and better reflects their properties that appear to be very similar in CTs without exposing patients to ionizing radiation. The structural explanation of MRI images leads to more precise volume definitions.[3] The organ at risk structures and tissues are identified in MRI images and registered with CT scan images. Unfortunately, this leads to systematic errors, extra costs, and prolonged scan time due to the availability and use of multiple modalities. However, one of the major limitations associated with the MRI only system is that the intensity values do not provide the electronic density. Various methods have been presented in articles for automatic generation of Pseudo-CT (P-CT) images from MR images: Voxel-based

* Corresponding author at: Department of Biomedical Engineering and Medical Physics, School of Medicine, Shahid Beheshti University of Medical Sciences, Tehran, Iran.
*E-mail address:* mostaar@sbmu.ac.ir (A. Mostaar).

https://doi.org/10.1016/j.rpor.2020.05.005
1507-1367/

(Ultrashort echo time (UTE) sequences and MRI standard sequences.), Tissue segmentation, and Atlas-based techniques. In the tissue segmentation method, the voxels divide the MR image into a discrete set of tissue types, such as air, fat, soft tissue, and bone and, finally, assign different values of numbers to each tissue using bulk density assignment.[4,5] Tissue segmentation is not a simple problem, and an MR image size is usually not large enough to separate all types of tissue.[6] In addition, usual MR sequences cannot separate the air from the bone. As a result, most tissue segmentation methods require the use of multiple MR sequences with specific protocols. These protocols can increase the time of image preparation. Some methods require manual determination of bone volume such that separate models can be created for different regions.[7]

Korsholm et al. suggested that the dose difference (DD) of 2% is acceptable as compared to dose error rate of 1% when using CT in heterogeneous programming.[8] A semi-computerized approach within the brain region is utilized for bone segmentation from the soft tissue region.[9] In another research, a totally atlas-based segmentation method is used for bone separation before making use of the bulk density approach.[10]

Hoogcarspel et al. observed increased dose errors,[11] because of the assignment of a single value for bone density instead of separating values to bone structures. Elsewhere, MRI-based digitally reconstructed radiograph (DRR) was compared to prostate and brain CT-derived DRRs, via the bulk density method in Ref.[12] In Atlas-based strategy, a standard MRI sequence is used to generate P-CT images. This ensures that the scan time is minimized patient's movements are less likely, and the scan protocol is applicable in a clinical setting. Such methods are very common because of their ability to generate and estimate reliable P-CT images using common MRI images.[13–15] The fact that no specific MRI sequence, such as dUTE, is required to estimate a P-CT is the strength of the atlas-based approach. Sjolund et al. observed that the atlas-based strategies are highly resistant to visual artifacts because of their dependence on previous training information. However, this method causes problems in case of large anatomical changes or pathological differences.[16] These problems can be resolved to a certain extent using multi-atlas approaches and designing an atlas fusion method which is resistant to the alignment error of the atlas.[16,17] The use of voxel-based techniques is another method to generate P-CTs, eliminate the need for precise matching of an MR input image to an atlas,[18–20] and no image segmentation is required if applied mathematics strategies are used. This could incorporate the utilization of specific sequences such as UTE imagery or standard sequences. High-quality P-CT images have been generated, but applying multiple sequences results in prolongation of scan time and, consequently, an increase in patient movement. In addition, the use of unusual sequences in most radiotherapy centers can be problematic. Johanson et al.[18] predicted CT images using the Gaussian Mixture Regression (GMR) method. The overall bone errors in prostate patients' P-CT were examined to test how these factors affected the dose calculations in Ref.[21] They also evaluated the prostatic DRRs derived from P-CT images.[22]

### 1.1. Aim

The aim of the present research is to estimate the P-CT images using MRI images in the design of external radiotherapy and treatment planning in the brain and head region. A voxel-based approach with regression models have been used in this research.

## 2. Materials and methods

The present study is carried out on real image data of 14 patients with brain tumor who will be randomly assigned (age range of 20–82 years, mean age of 50 years). Ten data are evaluated as train and validation data and 4 are selected as blind test data. The parameters of MR images taken from 10 patients by a 1.5-Tesla scanner (Avanto, Siemens) were as follows: echo time 9 ms, repeat time 300 ms, 20-degree flip angle, 512 × 512 mm field of view (FOV). CT images of each person taken by Siemens scanner were as follows: voltage = 100–120 kV, radiation = 300 mAs, resolution = 0.5 × 0.5 mm, and slice thickness = 1 mm. The blind data are not used in the regression model training process. These data have different control parameters such as TR and TE value (TR: 300–500 ms, TE: 8–17) as shown in Table 1. They were achieved from different health centers to show the ability of the generalizability of the proposed algorithm.

The patient's head will be held stable by a mask throughout the entire period. As a pre-processing step in this article, optimization algorithms were used, where PSNR and MSE can be defined as an objective function.[23] Furthermore, the training of a regression model on unaligned data seems very important, as every single voxel in MRI exactly correlates with the same voxel in CT. Then, the sets of CT and MRI images are segmented by the Fuzzy C-Means (FCM) algorithm into various classes, such as soft tissue (brain), air, and bone. The main fundamental difference between the fuzzy clustering approach and the classic methods is that one sample can belong to more than one cluster.[24] The first approach is to design a model based on the brightness intensity values in both MRI and CT images. Voxels are uniformly selected from a volume of segmented tissue. The corresponding Hounsfield Unit (HU) and MRI intensity values from a voxel create a data point for generating and validating the model. This is done separately for each segment (bone, air, soft tissue). The second approach involves designing a model based on the statistical and texture features of the images. Further, a feature vector is formed for each segmented part. First-order statistical indices are calculated directly from the gray level values of pixels of the original image, regardless of their inter-spatial relationship. Typically, the first-order statistical indices are derived from the calculation of the statistical moments of the image histogram. In Eq. (1). $p(z_i)$ represents the number of pixels in the image that have a level equal to $z_i$. The normalized histogram of $p(z_i)$ is obtained through dividing this value by the total number of image pixels according to the following equation:

$$p(z_i) = (p(z_i))/\sum_{i=1}^{L}(p(z_i) \quad (1)$$

**Table 1**
MR and CT parameters in training and test datasets.

| Data | Number of samples | MRI parameters | | | | CT parameters | | |
|---|---|---|---|---|---|---|---|---|
| | | Field strength | TE | TR | Flip angle | Voltage | Slice thickness | Tube current |
| Train and validation data | 10 | 1.5T | 9 ms | 300 ms | 20 | 100–120 KV | 2 | 230 |
| Blind test | 4 | 1.5T | 10 | 400 ms | 20 | 100–120 KV | 2 | 284 |
| | | 1.5T | 8 | 330 ms | 90 | 100–120 KV | 2 | 430 |
| | | 1.5T | 9.2 | 520 ms | 90 | 100–120 KV | 2 | 400 |
| | | 1.5T | 17 | 552 ms | 90 | 100–120 KV | 3 | 150 |

where $L$ represents the number of gray levels in the image. The normalized histogram can be considered as a probability density function and can be described by computing various statistical indices, such as mean, standard deviation and entropy, third-order moment, uniformity, and smoothness of image texture features. However, it does not provide any information on the relative spatial relationship between the gray-level values of pixels because of the lack of sensitivity to the pixel displacement of the image.[25] Polar coordinates can also be considered as an independent feature in the training phase because of the uniformity of the pixel brightness values in the brain CT scans and similarity between the bone area and air region in MRI. A point in Cartesian and polar coordinates can be converted to one another as follows:

$$x = r\cos\theta y = r\sin\theta \quad \theta = \begin{cases} \arctan\left(\frac{y}{x}\right) & \text{if } x > 0 \\ \arctan\left(\frac{y}{x}\right) + \pi & \text{if } x < 0 \text{ and } y \geq 0 \\ \arctan\left(\frac{y}{x}\right) - \pi & \text{if } x < 0 \text{ and } y < 0 \\ \frac{\pi}{2} & \text{if } x = 0 \text{ and } y > 0 \\ \frac{-\pi}{2} & \text{if } x = 0 \text{ and } y < 0 \end{cases} \quad (2)$$

Second-order statistical indices consider the relationship between gray-level values of the two pixels at a given distance and direction. They are often extracted based on the image co-occurrence matrix.[25] The co-occurrence matrix can be considered as a probability density function, which analyses the image texture by computing various statistical indices such as contrast and entropy, maximum uniformity probability (energy), and homogeneity of this matrix. The third-order statistical moment indicates the degree of Histogram skewness and the entropy being the criteria of randomized distribution of gray-level pixel of the image. The gray-level run length matrix (GLRLM) provides an appropriate means for calculating the third-order statistical indices and above.[26] Normalized run length matrix can be considered as a probability density function, which extracts the texture features of the image by calculating various indices such as short repeat power, non-uniform gray levels, and repeat rates. These features, along with the brightness level of the MR image, are mapped inputs, while the function output is the CT intensity value. In other words, we have a function proportional to the number of features rather than to an output.

$$I_{ctij} = f(I_{MR1ij} \cdot F_{MR2ij} \cdots\cdots F_{MR6ij} \cdots F_{MRnij}) \quad (3)$$

In this relationship, ($i$) and ($j$) represent each pixel of patient's datasets. ($F$) represents the features of the MR images, ($I$) shows the brightness value of these images, and ($n$) denotes the number of features. In addition, ($f$) indicates the regression function. Initially, we used the linear regression model to find the relationship between the MRI voxel and CT. Fig. 1 depicts the flowchart of the proposed methods.

The polynomial order is selected based on the minimum mean value of absolute error between the P–CT signal and CT simulation. The first and second-order polynomial equations are given to the system for the situation where the MRI intensity value is the only feature, which is presented to the regression model. The first model equation is as follows: $CT_{intensity} = B + A\ MR_{intensity}$ (Brain: A = −0.0109; B = 1061.9; Skull: A = 0.29; B = 2276.6; Air: −0.0011; B = 63.2), and the second model equation is $CT_{intensity} = C + B\ MR_{intensity} + A\,MR^2_{intensity}$ (Brain: A = 1.72e−05, B = −0.02, C = 1063; Skull: A = −5.2e−05, B = 0.035, C = 2282.9; Air: A = −6.15e−07; B = 0.0012; C = 62.7).

The following three models are presented based on the MRI intensity and the polar coordinate feature with their parameters as a sample in equations number 4, 5, 6. This procedure is repeated on the other types of features.

$$CT_{intensity} = D + C\theta + Br + A\ MR_{intensity} \quad (4)$$

- *Brain*: (A = −0.014, B = 0.014, C = 3.34, D = 1053.9); *Skull*: (A = −0.0051, B = 0.038, C = −23.61, D = 2283.5); *Air*: (A = −0.0012, B = 0.0057, C = −0.32, D = 61.81).

$$CT_{intensity} = G + F\theta + Er + D\ MR_{intensity} + C\theta^2 + Br^2 + A\,MR^2_{intensity} \quad (5)$$

- *Brain*: (G = 1048.5, F = 25.41, E = 0.0021, D = −0.014, C = −12.73, B = −1.148e−05, A = 4.07e−06); *Skull*: (G = 2447.4, F = −245.67, E = −0.5; D = 0.01, C = 148.35, B = 0.0006, A = 8.5e−06); *Air*: (G = 83.34, F = −9.72, E = −0.09; D = −0.0067, C = 5.8, B = 0.00012; A = 5.1e−06).

$$CT_{intensity} = G + F\theta + Er + DMR_{intensity} + C(r\theta) + B(\theta MR_{intensity}) + A\ rMR_{intensity} \quad (6)$$

- *Brain*: G = 1060.9, F = 8.33, E = 0.022; D = −0.085, C = −0.045, B = 0.051; A = 7.9e−05; *Skull*: (G = 2126.4, F = 131.3, E = 0.40; D = 0.46, C = −0.38, B = −0.109; A = −0.0007); *Air*: G = 58.04, F = 8.24, E = 0.015; D = −0.009, C = −0.02, B = −0.005; A = 1.4e−05.

Some of the usual evaluation criteria for the quality of a P-CT image are presented further. Perhaps the simplest and most commonly used criterion is to measure the voxel-wise mean absolute error and the mean error.

$$MAE_{vox} = \frac{1}{N}\sum_{n=1}^{N}|CT(n) - sCT(n)| \quad (7)$$

$$ME_{vox} = \frac{1}{N}\sum_{n=1}^{N}(CT(n) - sCT(n)) \quad (8)$$

The most important measure of the quality of P-CT images is the precise dosimetry measurement. Evaluation can be carried out by designing a P–CT-compatible treatment plan and then transferring the plan to the main CT and recalculate it using parameters of the same plan. The 3D distribution of the dose for a tumor volume or an OAR can be summed up in an interpretive mode using the so-called dose-volume cumulative histogram (DVH).

DVH indicates the minimum dosage received by a percentage of the tissue. The RayPlan treatment planning system (RaySearch laboratory, Stockholm, Sweden) is used to calculate the three-dimensional dose distribution and to obtain a dose-volume cumulative histogram. In this system, scalp regions, the organs at risk, and ultimately the tumor area must first be identified. Five eye regions, optical nerves, chiasma, and brain stem are selected as areas at risk. In order to determine the tumor area, the three areas of GTV, CTV, and PTV are also selected. Then, the registration operation is performed on MRI images as well as the P-CT and reference CTs such that these areas are accurately aligned on the P–CT images. This is performed to optimize the dose distribution operation. An appropriate plan mostly involves the left, right, vertebral, and lateral beams, which are considered for each patient, which is proportional to the tumor area for optimizing radiotherapy at appropriate angles. In order to perform three-dimensional dose distribution, the blocking process in the PTV region is done to avoid radiation of excessive doses to other healthy areas. Also,

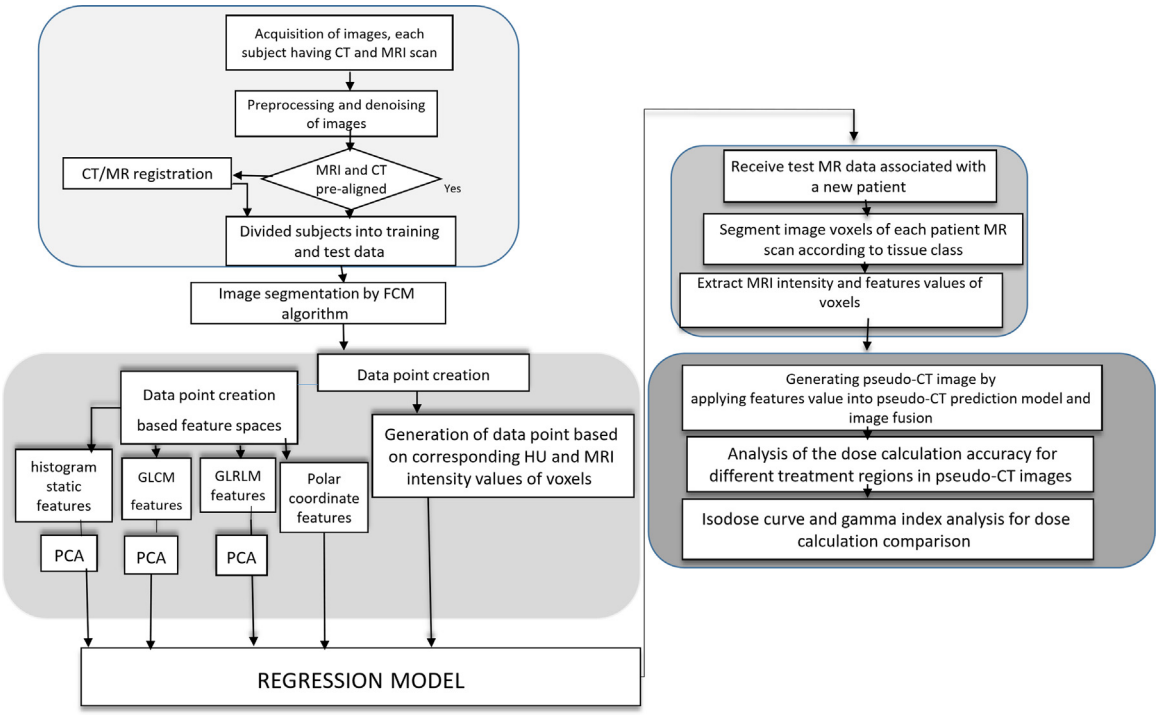


**Fig. 1.** Flowchart of the proposed.

the accuracy of the calculated dose of photon beams in the treatment planning system has been assessed based on the International Atomic Energy Agency protocol TEC-DOC 1583 on Computerized Imaging Reference Systems (CIRS) phantom. This protocol is known as the standard method for assessing the accuracy of computations in the treatment planning system. This treatment planning system has passed all the tests of this protocol. In addition, in order to compare the distribution of doses obtained in radiotherapy approaches, Gamma index is used to compare the consistency and uniformity of the dose distribution.

Low et al.[27] presented a method for comparing the measured dose distribution and calculating the dose distribution using the dose difference (DD) and distance-to-agreement (DTA). Therefore, some limitations are defined in DD and DTA with 2% or 3% difference in tolerance or 2 or 3 mm off the Isodose lines.

## 3. Results

The results of the proposed algorithm were evaluated by various methods such as the Mean Absolute Error (MAE), Mean Error (ME), Structural Similarity Index (SSIM), dose-volume histogram (DVH), Isodose curves, and gamma analysis. The MAE indicates an evaluation of the overall quality of the P-CT, while the ME can indicate whether there is a bias regarding under- or overestimation of the CT value. Then, 4 slices are presented as sample image after applying the introduced relationships to illustrate them more precisely in Fig. 2. Also, the results of ME and MAE errors based on the intensity and feature based methods (the images obtained from each group of features are fused together and a final image is formed) are shown in Fig. 2(h and i). According to Fig. 2, an MRI image as a P-CT image has a better view of the tumor region than the reference CT image. However, physicians often have to fuse MRI and CT images for a better view of the tumor region in conventional radiotherapy systems since CT images cannot display these areas well because of their low contrast. Considering this example image, it can be stated that a P–CT which is made from an MRI image can partly resolve this defect in CT images and eliminate the need for fusion. The reason is that P–CT images must have the ability to display non-uniform regions in tissues such as brain tissue in MR-based systems due to the absence of CT images. In Fig. 2(e–g), the difference between two P–CT and CT images is shown along with a structural similarity index.

Following another evaluation method, five eye regions, optical nerves, chiasma, and brain stem are selected as areas at risk with tumor area, as GTV, CTV, and PTV are also selected.

Fig. 3 reveals a plan on the CT, p-CT, and MR images. One of the capabilities of the RayPlan software is the ability to perform dose distribution calculations on MR images presented below for two patients as an example. It can be seen that these two curves are aligned with each other largely by comparing the DVH curve drawn. An estimation of the similarity between the two calculations is also obtained by comparing the points in the DVHs results obtained from the dose distribution calculation by CT and P-CT images. Fig. 3 displays the CTV, PTV, and GTV comparison between these groups of images at 7 points of dose distribution based on the volume.

Table 2 shows the comparison between D95, D50, and also the Absolute Relative Dose Difference (ARDD) of the reference CT, P-CT, and MR.

For the last evaluation part, Fig. 4 shows a sample of the results of the dose distribution for different absorption percentages. It shows dose distribution in a coronal, sagittal, and transversal view in CT and pseudo-CT by VERISOFT software. In order to compare the DD and DTA, two dose distributions, one as the reference dose distribution and the other as compared dose distribution, are usually selected. The aim of these assessments is to determine to what extent the compared dose distribution is similar to the reference dose distribution.

## 4. Discussion

Note that despite the existence of diverse methods in this area, there is an inconsistency within the criteria used to evaluate the pseudo CT quality and accuracy and this should be considered for comparing the methods. First, the stage of data pre-processing as

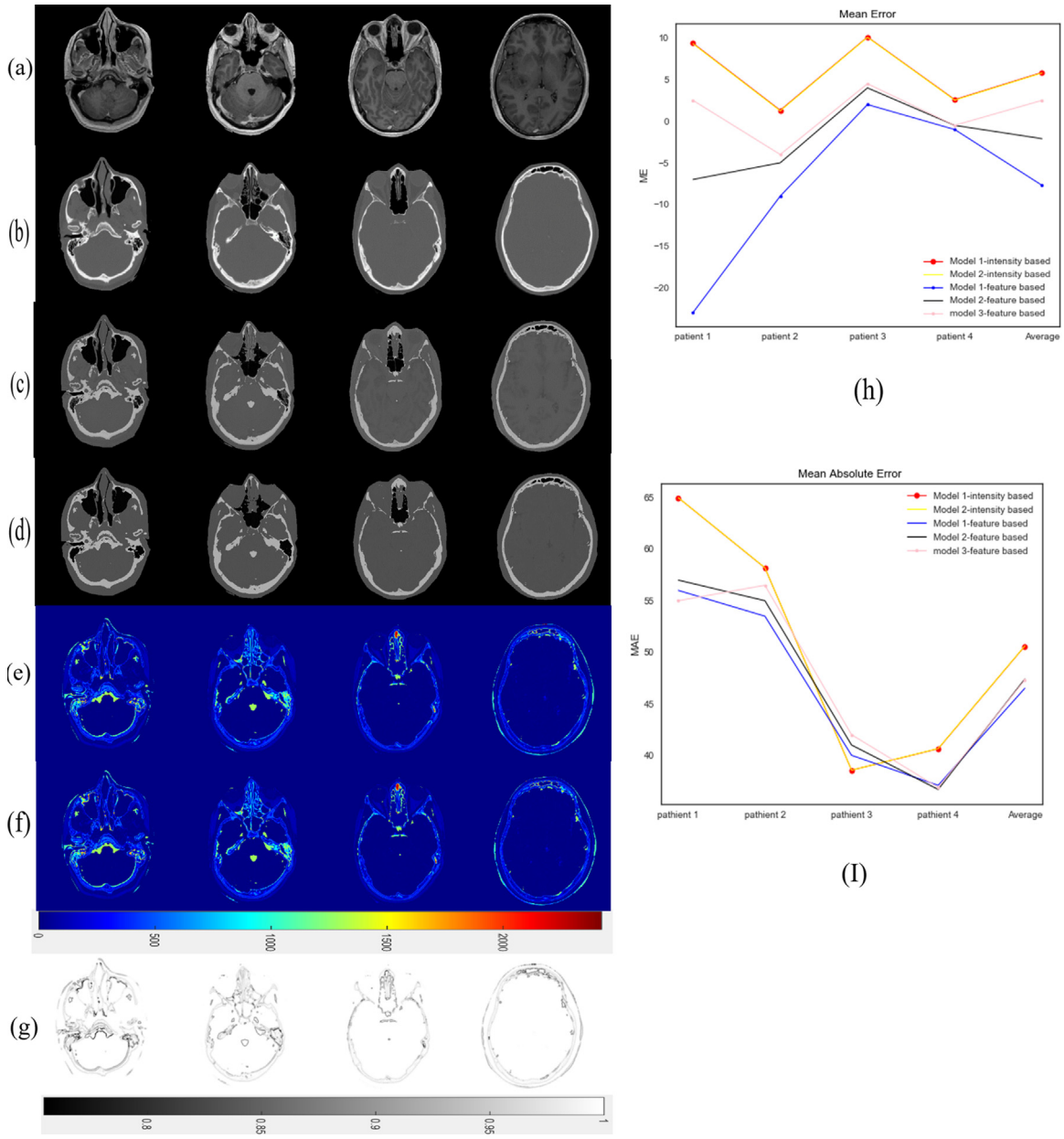


**Fig. 2.** (a and b) indicates the original MRI and CT slices, (c and d): P-CT images based on the fusion of different groups of features, Image (e and f) represents the differences between the original and pseudo-CT and image (g) the SSIM images in feature based approach. (h and i): MAE and ME error on the intensity based models among test subjects and their total average.

well as the choice of patient will affect the reported results. In addition, the aspects of the treatment method, the beam quality, purpose, and variability of OAR influence the dosimetric results. The mean absolute error (MAE) given the appropriate voxels chosen is a common reporting method for P–CT comparison purposes. Researches have suggested that a public database containing MRI and CT images for different parts should be presented with the advantage of eliminating the difference between pre-processing approaches.[28]

Different studies have reported different parameters, such as the mean absolute error in HU values, dose calculation changes, and DVH parameters for the intended region in the patient, as well as the percentage change in PTV parts for dosimetric comparison between P-CTs with CT. Gamma analysis[27] was used to evaluate the similarity of dose distribution between the P-CTs with CT in many studies. In clinical studies that are merely based on MRI planning, a larger group of patients should be tested for MRI. For ensuring that a wide range of patient anatomies are tested, a study with a sample size of larger than 100 patients with prostate cancer is currently ongoing in Sweden.[30] However, the acceptance rate for gamma distribution depends on a variety of factors, including DD and DTA. This number of variables makes it difficult to make a direct comparison between different studies. For example, the average acceptance rate of 97% is clinically acceptable for gamma criteria of 1%/1 mm in Ref.,[13] however, the acceptance rate of 94% should be considered, though this applies only to their criteria and method.

They assessed MAE values for different parts as MAEs have higher values in pseudo images in the brain region compared to prostate images. This is because of the difference in soft tissue as compared to the air and bone. It seems that the problem was reported through comparisons even in the case where the same

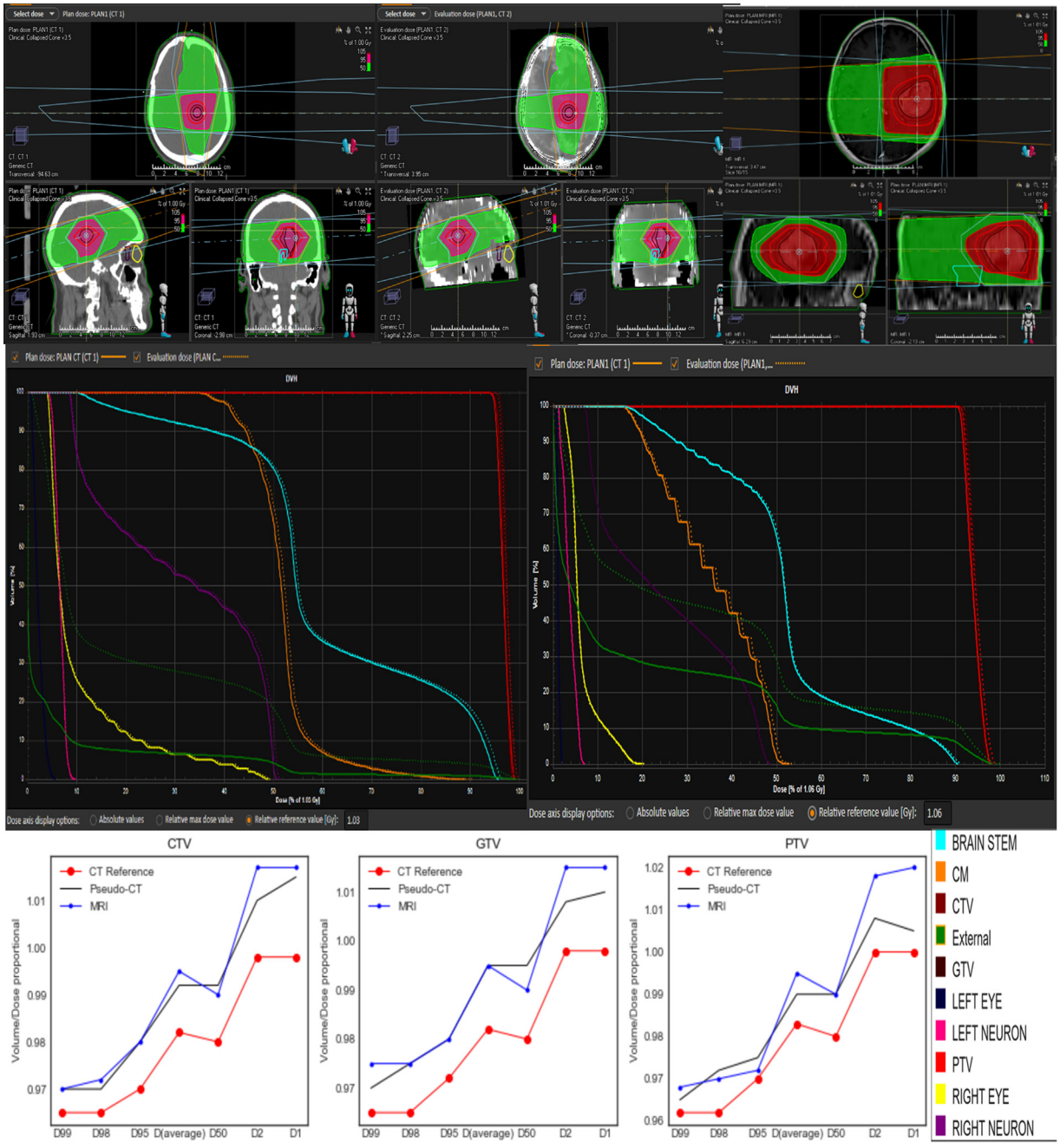


**Fig. 3.** first t line a sample plan on 2 patients on the original CT,P-CT and MR of the patients respectively; in second rows the DVHs of pseudo-CT are shown by the dashed line (. . .) and DVHs of the reference CT are represented by the solid line (___); A sample plan on the MR images of the patients. Last rows of Figure show the CTV, PTV, and GTV comparison between CT, P-CT and MRI groups of images at 7 points of dose distribution based on the volume (dose 99%–98%–95% – average – 50%–2%–1%). methods.

criteria and parameters were used. MAE values of about 40 HU are reported for the prostate, but 80–200 HU for the brain. However, low MAE values have been recently reported for the brain.[28] Gudur et al.[29] used a voxel-based technique with T1-weighted images and the Bayesian framework mean and absolute error value was equal to 126 HU Kapanen,[7] MAE of 135, Korhonen,[21] MAE of 11 HU for soft tissue and 99 HU for bone with PTV dose difference of <0.8%. 92% passed gamma analysis, Koivula et al.,[31] MAE of 34 HU for the brain and 42 HU for the prostate with 1.4% (brain), 0.6% (prostate) (cf.1.8%, 8.9% in the brain and 1.2%, 3.6, >91% passed gamma criteria, and Johansson et al.,[19] MAE of 130–140 HU and dose difference of 0.9–1.5 were reported. In this study, there was no need for specific protocols and multiple MR series for constructing P-CT images and CT replacement.

Regression relationships were obtained between the intensity of MRI images and the relative electron density of the P-CT through polynomial regression models. The structural similarity (SSIM) index values in these images also reported good results. Images were analyzed for mean/absolute error rate, gamma analysis, and mean absorbed dose. In presented approaches, the ME of 5.791 and 1.125, and MAE of 50.607 and 47.43 have been achieved in intensity-based and feature-based method, respectively.

The gamma pass rates were calculated for three different dose cubes of sagittal, coronal, and transversal on two DTA/DD value of 2 mm and 3 mm with these 2 approaches. In sagittal dose cube, we

**Table 2**
The comparison between D95 and D50 of the reference CT, P-CT and MR.

| ROI | D95% | | D50% | | ARDD (%) | |
|---|---|---|---|---|---|---|
| | CT | Pseudo CT | CT | Pseudo CT | D95 | D50 |
| Brain stem | 0.39 ± 0.19 | 0.395 ± 0.197 | 0.68 ± 0.16 | 0.685 ± 0.17 | 1.26 | 0.72 |
| Chiasma | 0.20 ± 0.14 | 0.2175 ± 0.149 | 0.33 ± 0.18 | 0.332 ± 0.18 | 7.83 | 0.6 |
| CTV | 0.97 ± 0.02 | 0.98 ± 0.021 | 0.98 ± 0.017 | 0.992 ± 0.01 | 1.02 | 1.2 |
| GTV | 0.972 ± 0.02 | 0.98 ± 0.021 | 0.98 ± 0.017 | 0.995 ± 0.019 | 0.81 | 1.5 |
| Left Eye | 0.01 ± 0 | 0.01 ± 0 | 0.015 ± 0.005 | 0.015 ± 0.005 | 0 | 0 |
| LON | 0.02 ± 0.017 | 0.0275 ± 0.017 | 0.04 ± 0.02 | 0.04 ± 0.02 | 27.2 | 0 |
| PTV | 0.97 ± 0.018 | 0.975 ± 0.017 | 0.98 ± 0.017 | 0.99 ± 0.014 | 0.51 | 1.01 |
| Right Eye | 0.035 ± 0.012 | 0.035 ± 0.01 | 0.057 ± 0.015 | 0.0575 ± 0.01 | 0 | 0.86 |
| RON | 0.077 ± 0.012 | 0.0775 ± 0.02 | 0.23 ± 0.112 | 0.235 ± 0.11 | 0.649 | 2.12 |

| ROI | D95% | | D50% | | ARDD (%) | |
|---|---|---|---|---|---|---|
| | CT | MRI | CT | MRI | D95 | D50 |
| Brain stem | 0.39 ± 0.19 | 0.377 ± 0.19 | 0.68 ± 0.16 | 0.645 ± 0.18 | 3.44 | 5.42 |
| Chiasma | 0.20 ± 0.14 | 0.202 ± 0.15 | 0.33 ± 0.18 | 0.32 ± 0.18 | 0.99 | 3.125 |
| CTV | 0.97 ± 0.02 | 0.98 ± 0.0082 | 0.98 ± 0.017 | 0.99 ± 0.01 | 1.02 | 1.01 |
| GTV | 0.972 ± 0.02 | 0.98 ± 0.0082 | 0.98 ± 0.017 | 0.99 ± 0.01 | 0.81 | 1.01 |
| Left Eye | 0.01 ± 0 | 0.01 ± 0 | 0.015 ± 0.005 | 0.015 ± 0.005 | 0 | 0 |
| LON | 0.02 ± 0.017 | 0.027 ± 0.017 | 0.04 ± 0.02 | 0.04 ± 0.02 | 25.9 | 0 |
| PTV | 0.97 ± 0.018 | 0.972 ± 0.005 | 0.98 ± 0.017 | 0.99 ± 0.01 | 0.2 | 1.01 |
| Right Eye | 0.035 ± 0.012 | 0.03 ± 0.009 | 0.057 ± 0.015 | 0.05 ± 0.02 | 16.6 | 0.14 |
| RON | 0.077 ± 0.012 | 0.075 ± 0.031 | 0.23 ± 0.112 | 0.21 ± 0.1 | 2.6 | 9.5 |

*ARDD: absolute relative dose difference; LON: left optic nerve; RON: right optic nerve.

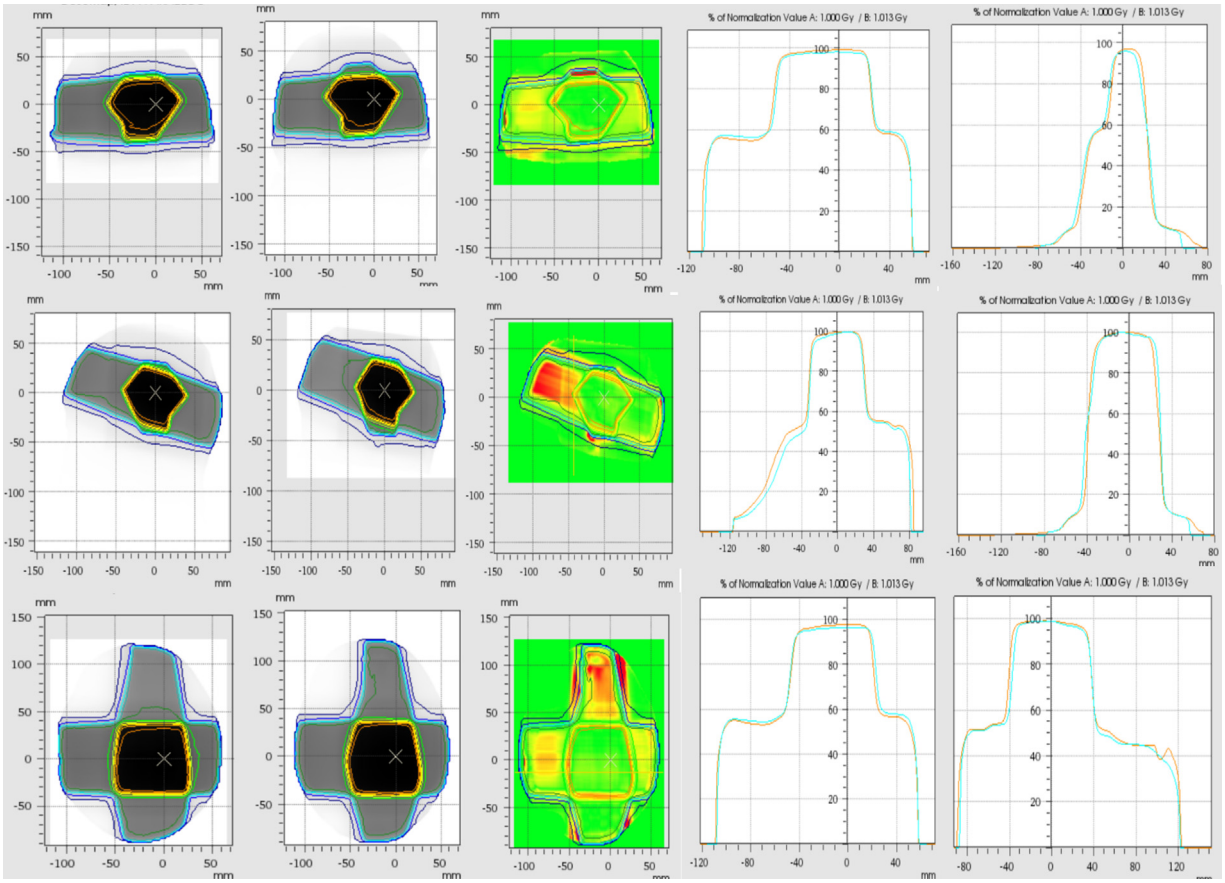


**Fig. 4.** Dose distribution in coronal, sagittal, and transversal view in CT and pseudo-CT by VERISOFT software (PTW Company, Germany).

have gotten 86.4 ± 4.05 (Mean ± Std) and 91.5 ± 4.37 in intensity based and 87.6 ± 1.72 and 92 ± 2.10 in feature based approach in DTA/DD of 2 mm and 3 mm, respectively, among 4 test patients. In addition, in the coronal view with DTA/DD of 2 and 3 mm, the gamma pass rate of 90.1 ± 1.62, 95.4 ± 1.9 in intensity based and 85.8 ± 3.27, 93.7 ± 1.98 in feature based model was achieved. At last, we have gotten 84.8 ± 3.66, 90.7 ± 4.58 in intensity-based model and 84.5 ± 5.31, 91 ± 5.02 in the feature based model for the transversal dose cube view. The overall PTV absolute dose difference in D95, D50 were 0.51, 1.01 in the feature-based method.

## 5. Conclusion

In this study, there was no need for specific protocols and multiple MR series for constructing P-CT images and CT replacement. Regression relationships were obtained between the intensity of MRI images and the relative electron density of the artificial CT through polynomial regression models. The structural similarity (SSIM) index values in these images also reported good results. Images were analyzed for mean/absolute error rate, gamma analysis, and mean absorbed dose. The present research reported overall an appropriate error rate compared to similar methods in voxel-based articles.

## Conflict of interest

None declared.

## Financial disclosure

None declared.

## Acknowledgments

This article was derived from the Ph.D. thesis of Niloofar Yousefi Moteghaed in the Biomedical and Medical Physics Department at the Shahid Beheshti University of Medical Sciences. (Registration No. 140M).

## References

1. Khoo VS, Joon DL. New developments in MRI for target volume delineation in radiotherapy. *Br J Radiol*. 2006;79:S2–S15.
2. Schmidt MA, Payne GS. Radiotherapy planning using MRI. *Phys Med Biol*. 2015;60:R323.
3. Kristensen BH, Laursen FJ, Logager V, et al. Dosimetric and geometric evaluation of an open low-field magnetic resonance simulator for radiotherapy treatment planning of brain tumours. *Radiother Oncol*. 2008;87:100–109.
4. Zaidi H, Montandon ML, Slosman DO. Magnetic resonance imaging-guided attenuation and scatter corrections in three-dimensional brain positron emission tomography. *Med Phys*. 2003;30:937–948.
5. Catana C, van der Kouwe A, Benner T, et al. Toward implementing an MRI-based PET attenuation-correction method for neurologic studies on the MR-PET brain prototype. *J Nucl Med*. 2010;51:1431–1438.
6. Hsu SH, Cao Y, Huang K, Feng M, Balter JM. Investigation of a method for generating synthetic CT models from MRI scans of the head and neck for radiation therapy. *Phys Med Biol*. 2013;58:8419.
7. Kapanen M, Tenhunen M. T1/T2*-weighted MRI provides clinically relevant pseudo-CT density data for the pelvic bones in MRI-only based radiotherapy treatment planning. *Acta Oncol*. 2013;52:612–618.
8. Korsholm ME, Waring LW, Edmund JM. A criterion for the reliable use of MRI-only radiotherapy. *Radiat Oncol*. 2014;9:16.
9. Stanescu T, Hans-Sonke J, Stavrev P, et al. 3T MR-based treatment planning for radiotherapy of brain lesions. *Radiat Oncol*. 2006;40:125–132.
10. Stanescu T, Jans HS, Pervez N, et al. A study on the magnetic resonance imaging (MRI)-based radiation treatment planning of intracranial lesions. *Phys Med Biol*. 2008;53:3579.
11. Hoogcarspel SJ, Van der Velden JM, Lagendijk JJ, et al. The feasibility of utilizing pseudo CT-data for online MRI based treatment plan adaptation for a stereotactic radiotherapy treatment of spinal bone metastases. *Phys Med Biol*. 2014;59:7383.
12. Weber DC, Wang H, Albrecht S, et al. Open low-field magnetic resonance imaging for target definition, dose calculations and set-up verification during three-dimensional CRT for glioblastoma multiforme. *Clin Oncol*. 2008;20:157–167.
13. Andreasen D, Van Leemput K, Edmund JM. A patch-based pseudo-CT approach for MRI-only radiotherapy in the pelvis. *Med Phys*. 2016;43:4742–4752.
14. Edmund JM, Andreasen D, Mahmood F, et al. Cone beam computed tomography guided treatment delivery and planning verification for magnetic resonance imaging only radiotherapy of the brain. *Acta Oncol*. 2015;54:1496–1500.
15. Demol B, Boydev C, Korhonen J, et al. Dosimetric characterization of MRI-only treatment planning for brain tumors in atlas-based pseudo-CT images generated from standard T1-weighted MR images. *Med Phys*. 2016;43:6557–6568.
16. Sjölund J, Forsberg D, Andersson M, et al. Generating patient specific pseudo-CT of the head from MR using atlas-based regression. *Phys Med Biol*. 2015;60:825.
17. Andreasen D, Van Leemput K, Hansen RH, et al. Patch-based generation of a pseudo CT from conventional MRI sequences for MRI-only radiotherapy of the brain. *Med Phys*. 2015;42:1596–1605.
18. Jonsson JH, Johansson A, Söderström K, et al. Treatment planning of intracranial targets on MRI derived substitute CT data. *Radiother Oncol*. 2013;108:118–122.
19. Johansson A, Karlsson M, Yu J, et al. Voxel-wise uncertainty in CT substitute derived from MRI. *Med Phys*. 2012;39:3283–3290.
20. Dowling JA, Sun J, Pichler P, et al. Automatic substitute computed tomography generation and contouring for magnetic resonance imaging (MRI)-alone external beam radiation therapy from standard MRI sequences. *Int J Radiat Oncol Biol Phys*. 2015;93:1144–1153.
21. Korhonen J, Kapanen M, Keyriläinen J, et al. Influence of MRI-based bone outline definition errors on external radiotherapy dose calculation accuracy in heterogeneous pseudo-CT images of prostate cancer patients. *Acta Oncol*. 2014;53:1100–1106.
22. Korhonen J, Kapanen M, Sonke JJ, et al. Feasibility of MRI-based reference images for image-guided radiotherapy of the pelvis with either cone-beam computed tomography or planar localization images. *Acta Oncol*. 2015;54:889–895.
23. Moteghaed NY, Mostaar A. Biomedical image denoising based on hybrid optimization algorithm and sequential filters. *J Biomed Phys Eng*. 2020;10:83–92.
24. Bezdek JC, Ehrlich R, Full W. FCM: the fuzzy c-means clustering algorithm. *Comput Geosci*. 1984;10:191–203.
25. Aggarwal N, Agrawal RK. First and second order statistics features for classification of magnetic resonance brain images. *J Signal Inf Process*. 2012;3:146.
26. Singh KH. A comparison of gray-level run length matrix and gray-level co-occurrence matrix towards cereal grain classification. *Int J Comput Eng Inf Technol*. 2016;7:9–17.
27. Low DA, Harms WB, Mutic S, et al. A technique for the quantitative evaluation of dose distributions. *Med Phys*. 1998;25:656–661.
28. Edmund JM, Nyholm T. A review of substitute CT generation for MRI-only radiation therapy. *Radiat Oncol*. 2017;12:28.
29. Gudur MS, Hara W, Le QT, et al. A unifying probabilistic Bayesian approach to derive electron density from MRI for radiation therapy treatment planning. *Phys Med Biol*. 2014;59:6595.
30. Persson E. Multi-center/multi-vendor validation of MRI only prostate treatment planning. In: *Presented at the 4th MR in RT Symposium*. 2016.
31. Koivula L, Wee L, Korhonen J. Feasibility of MRI-only treatment planning for proton therapy in brain and prostate cancers: dose calculation accuracy in substitute CT images. *Med Phys*. 2016;43:4634–4642.